Nanoscale

PAPER

View Article Online
View Journal | View Issue

Cite this: *Nanoscale*, 2016, **8**, 8228

3D dual-confined sulfur encapsulated in porous carbon nanosheets and wrapped with graphene aerogels as a cathode for advanced lithium sulfur batteries†

Yang Hou,‡ Jianyang Li,‡ Xianfeng Gao, Zhenhai Wen, Chris Yuan* and Junhong Chen*

Received 20th December 2015,
Accepted 14th March 2016

DOI: 10.1039/c5nr09037g

www.rsc.org/nanoscale

Although lithium–sulfur (Li–S) batteries have attracted much attention due to their high theoretical specific energy and low cost, their practical applications have been severely hindered by poor cycle life, inadequate sulfur utilization, and the insulating nature of sulfur. Here, we report a rationally designed Li–S cathode with a dual-confined configuration formed by confining sulfur in 2D carbon nanosheets with an abundant porous structure followed by 3D graphene aerogel wrapping. The porous carbon nanosheets act as the sulfur host and suppress the diffusion of polysulfide, while the graphene conductive networks anchor the sulfur-adsorbed carbon nanosheets, providing pathways for rapid electron/ion transport and preventing polysulfide dissolution. As a result, the hybrid electrode exhibits superior electrochemical performance, including a large reversible capacity of 1328 mA h g^{-1} in the first cycle, excellent cycling stability (maintaining a reversible capacity of 647 mA h g^{-1} at 0.2 C after 300 cycles) with nearly 100% Coulombic efficiency, and a high rate capability of 512 mA h g^{-1} at 8 C for 30 cycles, which is among the best reported rate capabilities.

1. Introduction

Lithium sulfur (Li–S) batteries have attracted enormous research interest in recent years due to their high theoretical capacity of 1672 mA h g^{-1} and theoretical energy density of 2600 W h kg^{-1}.[1–9] From a material perspective, sulfur has great commercialization potential due to its low cost, non-toxicity, environmental friendliness, and natural abundance.[10,11] However, with significant progress in research and development recently, some major challenges with Li–S batteries remain, such as: (I) poor electronic conductivity of sulfur, intermediate polysulfide species, and the final discharge product (Li_2S);[12–14] (II) severe dissolution and shuttling problems of polysulfides in the liquid electrolyte;[15,16] and (III) large volumetric expansion of sulfur during the lithium insertion/extraction processes.[17,18] These problems cause not only low utilization of elemental sulfur in the cathode but also poor cycling performance and inferior rate capability. To overcome these challenges, past efforts have focused on developing novel porous carbon–sulfur composite nanostructures. For example, meso/micro-porous core–shell carbon,[19] porous carbon nanospheres,[20,21] organic framework-derived carbon,[22,23] biomass derived activated carbon,[24] porous hollow carbon,[25,26] and spherical-ordered mesoporous carbon nanoparticles[27] have been developed and investigated as the host and conducting framework for suppressing the polysulfide diffusion while improving the electrical conductivity of the sulfur, based on their high surface area, abundant pore structure, and conductive carbon skeleton. Among these materials, the porous carbon nanosheet (PCN) with a unique two-dimensional (2D) architecture, large surface area, and highly porous structure has received intense attention and opened new possibilities for confining sulfur and trapping the soluble polysulfides.[28,29] However, these porous carbons are amorphous in general, and have relatively poor electrical conductivity, which limits the electron transfer and weakens their electrochemical activity to a certain extent.[30,31] Moreover, most existing synthesis procedures are somewhat complex and require several steps. Thus, it is necessary to develop a facile synthesis procedure for designing hybrid nanocarbons that combine highly conductive carbon nanomaterials with porous carbon nanosheets encapsulating sulfur (PCN-S) to obtain high-performance Li–S electrodes.

Department of Mechanical Engineering, University of Wisconsin-Milwaukee, 3200 North Cramer Street, Milwaukee, Wisconsin 53211, USA. E-mail: jhchen@uwm.edu, cyuan@uwm.edu

†Electronic supplementary information (ESI) available. See DOI: 10.1039/c5nr09037g

‡These authors contributed equally to this work.

Recently, three-dimensional (3D) graphene aerogels,[32–34] a family of 3D nanostructured porous carbons characterized with high porosity, large surface area, and excellent electronic conductivity, have been reported. In these aerogels, the unique 3D interconnected graphene frameworks can enhance the diffusion and transport of electrons and ions in the whole electrode;[35–37] simultaneously, the hierarchical porous structure of the 3D aerogel can facilitate the infiltration of the electrolyte and accommodate the volume expansion during the Li–S battery operation.[38,39] Therefore, it is anticipated that a new multifunctional nanostructured material combining the PCN and 3D graphene aerogel together to form a 3D hierarchical nanoarchitecture would be an excellent candidate for high-performance sulfur cathodes. When applied in a Li–S battery, an intimate face-to-face contact between the 2D PCN-S and graphene nanosheet aerogel would form and possibly enable the overall structural integrity and efficient electron and ion transportation across the interface when compared with 0D nanoparticles that are only in point-to-point contact.[40–42] To the best of our knowledge, such a hierarchical porous carbon-based hybrid aerogel for developing high-performance Li–S batteries has not yet been reported.

Here, we present a novel design and facile synthesis of a light-weight carbon-based cathode by confining sulfur in 2D carbon nanosheets with an abundant porous structure followed by 3D graphene aerogel wrapping (PCN-S/RGOAs). In this architecture, the interconnected graphene networks enable fast electron and ion transfer. The overall 3D hybrid aerogel can significantly improve the amount of sulfur loading while suppressing the polysulfide dissolution and shuttling in the electrolyte. As a consequence, the obtained PCN-S/RGOAs hybrid with 57.4 wt% sulfur content, when applied in an Li–S battery, exhibits an outstanding reversible capacity of 1328 mA h g^{-1} in the first cycle and high rate capability of 512 mA h g^{-1} at 8 C for 30 cycles, which is among the best reported rate capabilities (Table S1†).

2. Experimental

2.1 Synthesis of PCN

PCN was synthesized following a reported method with slight modification.[43] In brief, 1 g of potassium citrate was heated in a tubular furnace at 900 °C with a rate of 10 °C min^{-1}, and then maintained at 900 °C for 2 h under an Ar atmosphere to generate a carbonized material, which was further washed with 0.5 M H_2SO_4 solution for 10 h and repeatedly washed with distilled water to remove inorganic impurities.

2.2 Synthesis of PCN-S

The prepared PCN and commercial sulfur with a weight ratio of 1 : 3 were dispersed into 10 mL toluene and stirred magnetically with heating at 60 °C until completely dry. The resulting powder mixture was then transferred to the tube furnace and heated at 155 °C for 24 h under an Ar atmosphere in order to obtain the PCN-S composite.

2.3 Synthesis of PCN-S/RGOAs

Firstly, graphene oxide (GO) was synthesized through chemical exfoliation of graphite powder using a modified Hummers' method.[44] In a typical synthesis of the PCN-S/RGOAs, 120 mg PCN-S was gradually added to 20 mL GO solution (2.5 mg mL^{-1}). The mixture was stirred strongly and sonicated for 2 h. Then, the resulting stable suspension was transferred to a Teflon-lined autoclave, and hydrothermally treated at 180 °C for 12 h. After that, the PCN-S/RGO hydrogel was washed several times with distilled water and freeze-dried to obtain the PCN-S/RGOAs.

2.4 Characterization

The morphology and structure characterization of the samples were carried out *via* transmission electron microscopy (TEM, Hitachi H 9000 NAR) and field emission scanning electron microscopy (FESEM, Hitachi S-4800). Energy-dispersive X-ray (EDX) spectroscopy with elemental mapping (Hitachi S-4800) was carried out to visualize the location of each element. Powder XRD patterns were recorded on a Scintag XDS 2000 X-ray powder diffractometer with Cu Kα radiation (λ = 1.5418 Å). Surface and bonding characterization was carried out by X-ray photoelectron spectroscopy (XPS, HP 5950A with Mg Kα as the source) and Fourier transform-infrared spectroscopy (FTIR, Bruker Vector Fourier transform spectrophotometer). Raman spectra were recorded with a 633 nm laser excitation using a Renishaw 1000B Raman spectrometer. The BET specific surface area and pore-size distribution were measured by N_2 adsorption–desorption isotherm curves using a Micromeritics ASAP 2020 system. Thermogravimetric analysis (TGA, TA SDT 2960 thermoanalyzer) was carried out to determine the weight of the sulfur at a heating rate of 5 °C min^{-1} in an argon atmosphere.

2.5 Electrochemical measurements

The as-prepared samples were mixed with carbon black and polyvinylidene difluoride (1.5 wt% in *N*-methyl-2-pyrrolidone solution) in a weight ratio of 8 : 1 : 1 to form a wet slurry. The slurry was coated on aluminium foil and dried at 70 °C overnight under vacuum to yield a composite electrode. The sulfur content in the cathode electrode was controlled to a mass loading of 2 mg cm^{-2} (corresponding to a composite loading of ~3.5 mg cm^{-2}). CR2032-type coin cells were assembled with the composite as a working electrode and lithium foil as the counter electrode and reference electrode in an argon filled glove box with moisture and oxygen concentrations below 1.0 ppm. The separator was a Celgard-2320 membrane composed of 20 μm thick polypropylene (PP)/polyethylene/PP trilayers. The electrolyte was 1.0 M lithium bis (trifluoromethanesulfonyl)imide (LiTFSI) dissolved in 1,2-dimethoxyethane and 1,3-DOL containing $LiNO_3$ (1 wt%) solvents (1 : 1 v/v). Cyclic voltammetry (CV) between 1.7 and 3.0 V at a scan rate of 0.1 mV s^{-1} was performed on a LANHE CT2001A (Land, China) and the charge–discharge cycles were also performed within the same voltage range. All specific

capacities in this work were calculated based on the mass of active sulfur, which can be easily converted back to the capacity based on the mass of the PCN-S/RGOAs hybrid using our TGA data. AC impedance was measured on a VersaSTAT 3F (Princeton Applied Research, USA) for these cells in the frequency range from 100 KHz to 0.1 Hz with the amplitude of 5 mV.

3. Results and discussion

Fig. 1a shows a schematic synthesis of the PCN-S/RGOAs hybrid. First, the PCN was prepared by a direct carbonization and activation of potassium citrate under flowing argon and then acid etching of the impurities. Sulfur was subsequently impregnated into the PCN through a simple melt infiltration method to produce the PCN-S composite. Finally, the PCN-S/RGOAs was obtained by hydrothermal reaction using GO and PCN-S as precursors, followed by freeze-drying.

The structure and morphology of the samples were characterized using field emission scanning electron microscopy (FESEM). After sulfur encapsulation (Fig. S1 and S2†), the PCN-S maintains the original morphology and no sulfur particles are observed on the surfaces of the nanosheets, indicating that sulfur was fully diffused into the pore structure of the PCN. The FESEM images of the PCN-S/RGOAs show that a well-organized, highly porous 3D network microstructure was formed consisting of wrinkled graphene nanosheets and 2D PCN-S (Fig. 1b–e), with interconnected macro-pores of several-hundred nanometers in diameter. Such a hybrid framework in an Li–S battery can not only largely improve the ion diffusion and mass transfer,[45] but also can efficiently suppress the aggregation and restacking of PCN-S,[46] thereby enhancing the electrochemical activity and stability of the PCN-S/RGOAs.

X-ray diffraction (XRD) patterns confirmed the orthorhombic phase of sulfur in the PCN-S composite (Fig. S3†). After hydrothermal treatment, the intensity of the sulfur peaks became weak and an overlapping broad peak at about 26° appeared, which can be attributed to the successful introduction of RGOAs.[47] Thermogravimetric analysis (TGA) reveals that the sulfur content in the PCN-S/RGOAs hybrid is about 57.4 wt% (Fig. 1f). Moreover, the sulfur evaporation temperature of PCN-S/RGOAs was higher than that of PCN-S, suggesting a strong interaction between the PCN-S and RGOAs. The Raman spectrum of the PCN-S/RGOAs hybrid is shown in Fig. 1g. Three characteristic peaks centered at 150, 216, and

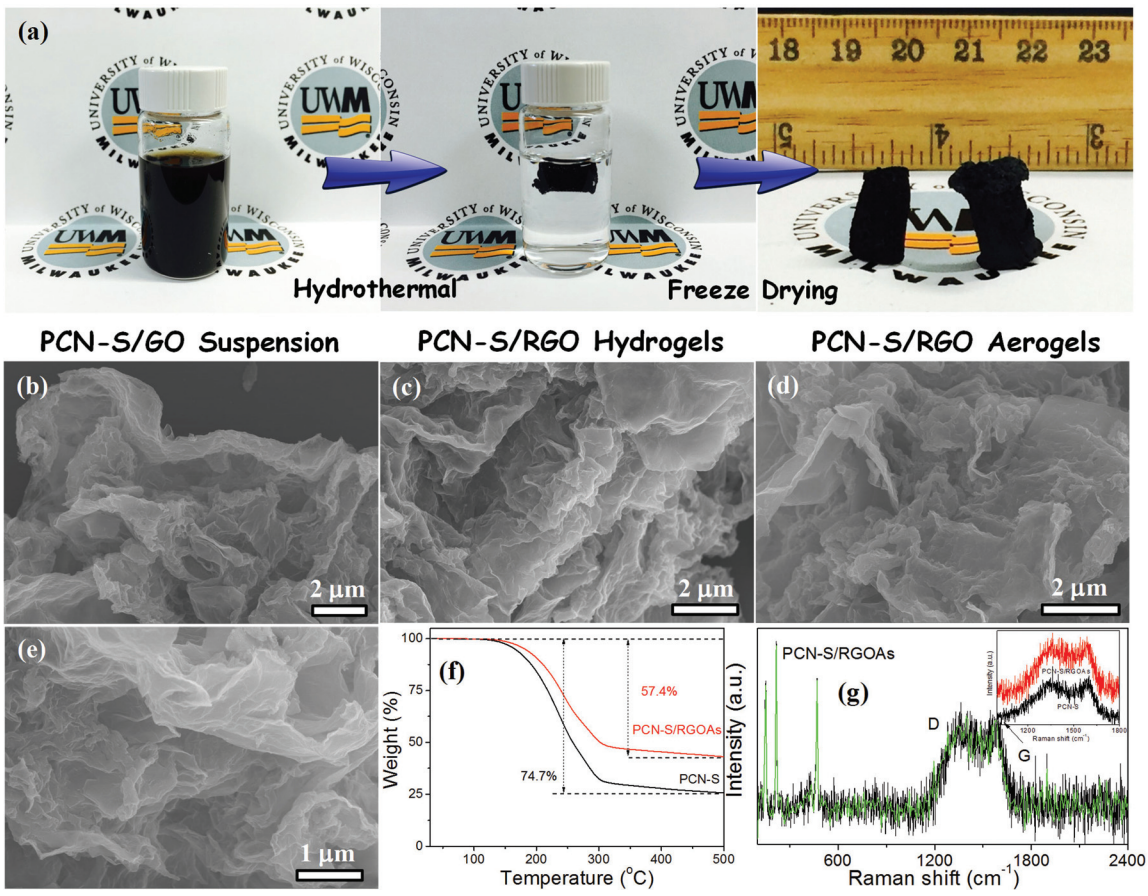

Fig. 1 (a) Schematic illustration of the synthesis process of PCN-S/RGOAs. (b–e) FESEM images of PCN-S/RGOAs. (f) TGA curves of PCN-S and PCN-S/RGOAs under Ar flow. (g) Raman spectra of PCN-S/RGOAs with those of PCN-S and PCN-S/RGOAs in the inset.

469 cm^{-1} are related to the E2, E3, and A1 symmetry modes of S–S bonds, respectively,[48] suggesting the presence of orthorhombic sulfur in the hybrid. The orthorhombic sulfur in the PCN-S/RGOAs is further measured and confirmed by Fourier transform infrared spectroscopy (FTIR, Fig. S4†). In addition, two broad Raman peaks are observed at about 1576 (G-band) and 1350 cm^{-1} (D-band), corresponding to the defects and sp^3 carbon networks in the hybrid, respectively.[49] The intensity ratio I_D/I_G of ~1.0 indicates its partial graphitic nature,[50] which favors the transport of electrons from/to the sulfur.

Fig. 2a shows a digital image of the monolithic PCN-S/RGOAs. The obtained hybrid is light and can stand on the top of a fluffy ball without breaking it (inset of Fig. 2a). Elemental mappings of C and S and their overlapping images show a well-matched spatial distribution of the two elements, and such a uniform distribution of sulfur indicates the successful incorporation of sulfur into the 3D carbon-based hybrid networks (Fig. 2b–e). The energy-dispersive X-ray (EDX) spectrum given in Fig. 2f further confirms the presence of dominant peaks for C, S, and O (note that Si is from the substrate, while Ir comes from the metal coating for the FESEM tests).

Furthermore, the TEM images reveal that the PCN-S maintains the 2D layered structure, but the contrast of the image becomes darker than that of pure PCN due to the sulfur impregnation (Fig. 3a and b). No large sulfur particles are observed in the PCN-S composite. Comparing Fig. 3b with Fig. 3c and d, it is clearly observed that the surfaces of the PCN-S/RGOAs exhibit different morphologies. The images clearly show that the crumpled graphene nanosheets cover the surface of the laminar structured PCN-S. The high-resolution TEM (HRTEM) image shows a distinguished and coherent interface between the PCN-S and graphene (the interlayer spacing of 0.34 nm, Fig. 3e), indicating that a close interfacial contact is formed, which is beneficial for facilitating the fast electronic and ionic transport and restricting the volume expansion and aggregation of sulfur nanoparticles.[51] An HRTEM image of the sulfur nanoparticles was not obtained because the nanoparticles sublimate very fast under electron beam irradiation;[52] however, the presence of sulfur in the hybrid can be verified by the corresponding EDX spectrum. As shown in the inset of Fig. 3e, the EDX spectrum of PCN-S/RGOAs displays a strong sulfur peak, around ten times that of carbon. The TEM image of bare RGOAs is also shown in Fig. 3f for comparison.

To investigate the surface chemical composition of the PCN-S/RGOAs, X-ray photoelectron spectroscopy (XPS) analysis was performed. The XPS spectrum clearly indicates that the hybrid includes three elements: C, S, and O (Fig. 4a). The C 1s spectrum in Fig. 4b shows five deconvoluted peaks. The main peak at 284.6 eV can be assigned to sp^2 hybridized carbon (C–C/C=C), and the small peaks centered at 285.6, 286.4, 287.2, and 289.3 eV contain contributions from different C–S, C–O, C=O, and O–C=O bonding configurations, respectively.[53,54] The successful loading of sulfur is evidenced by the S 2p spectrum of PCN-S/RGOAs (Fig. 4c). Two fitted peaks positioned at 163.4 and 164.5 eV correspond to the S $2p_{3/2}$ and S $2p_{1/2}$ spin–orbit levels of elemental sulfur, respectively. The minor peaks at 169.9–168.7 eV are attributed to the sulphate species formed by the oxidation of sulfur in air.[52] After sulfur impregnation, the Brunauer–Emmett–Teller (BET) specific surface area and the pore volume of the PCN-S decreased to 15 $m^2\ g^{-1}$ and 0.045 $cm^3\ g^{-1}$, respectively (Fig. S5†), indicating the successful migration of sulfur into the pores. We find a marked increase in the BET specific surface area to 43 $m^2\ g^{-1}$ when RGOAs is further introduced. A typical type IV isotherm with a H3 hysteresis loop demonstrates the mesoporous structure of the PCN-S/RGOAs (Fig. 4d).[55] Correspondingly, one peak centered at ~35 nm is found in the pore size distribution curve (inset of Fig. 4d).

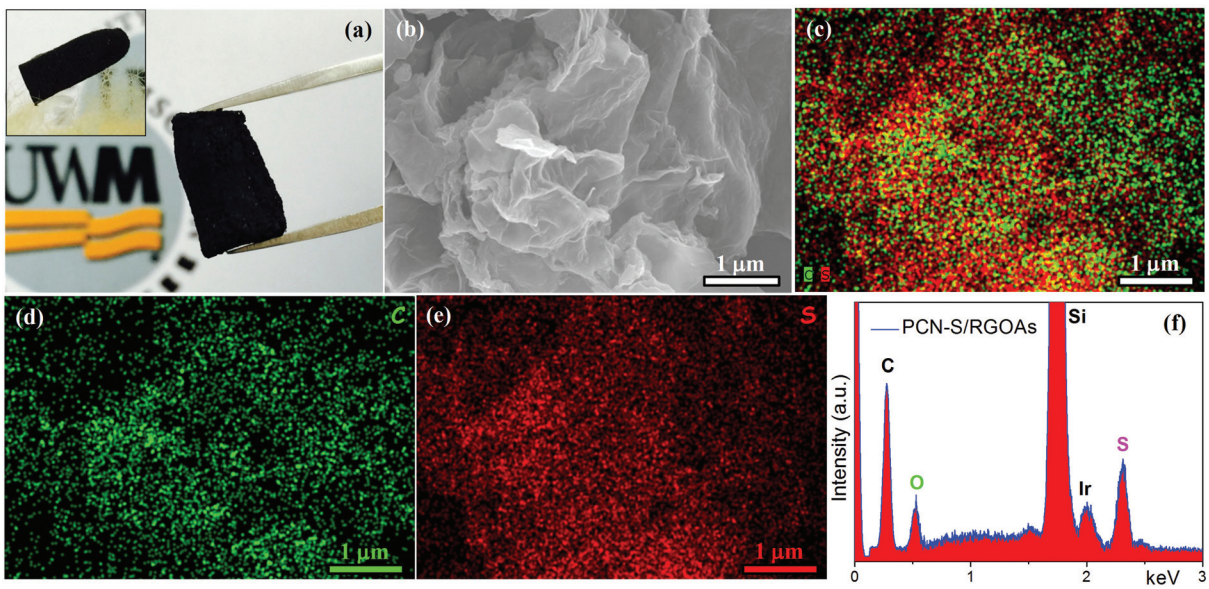

Fig. 2 (a) Appearance of PCN-S/RGOAs. FESEM image (b), elemental mappings (c–e), and EDX spectrum (f) of PCN-S/RGOAs.

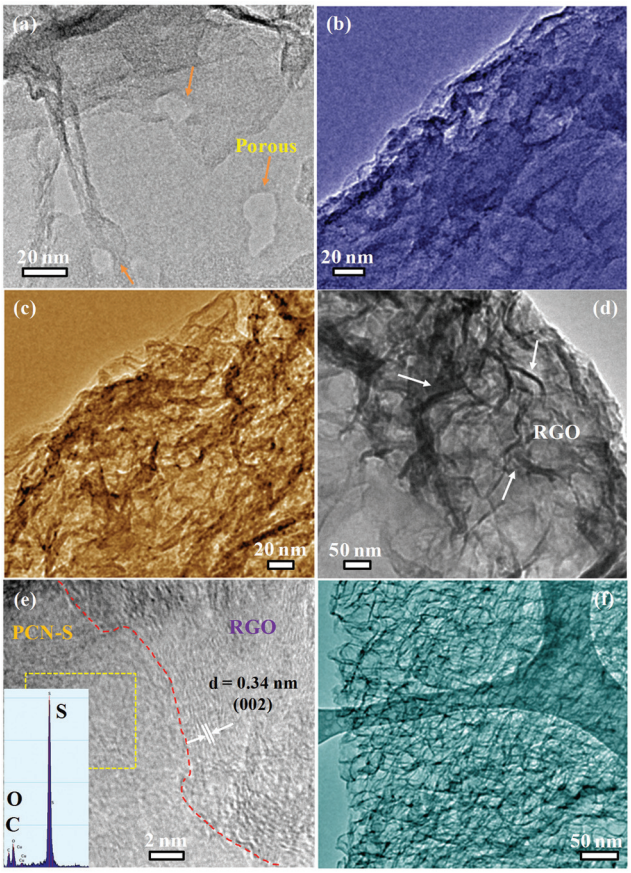

Fig. 3 TEM and HRTEM images of PCN (a), PCN-S (b), PCN-S/RGOAs (c–e), and RGOAs (f). Inset: the corresponding EDX spectrum from the area labeled by the rectangular box.

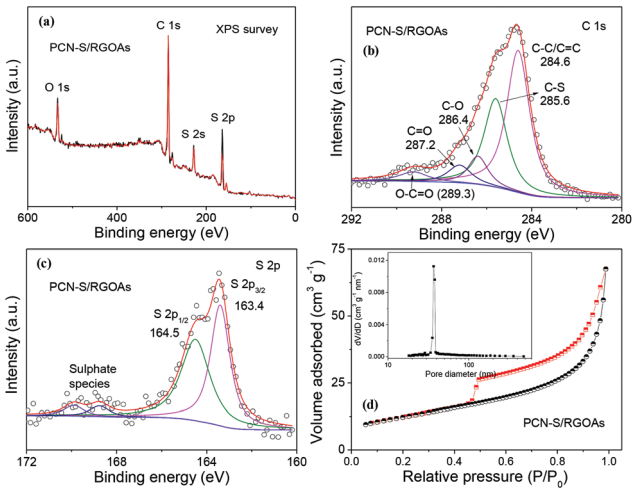

Fig. 4 The survey XPS spectrum (a), high-resolution C 1s XPS spectrum (b), high-resolution S 2p XPS spectrum (c), and nitrogen adsorption isotherm plot (d) of PCN-S/RGOAs. Inset: BJH pore size distribution of PCN-S/RGOAs.

The cyclic voltammetry (CV) curves of the PCN-S/RGOAs hybrid in the potential window of 1.7 V–3.0 V, at a scanning rate of 0.1 mV s^{-1}, depict two distinguished reduction peaks and two overlapping oxidation peaks due to the multistep reaction mechanism of sulfur with Li^+ ions (Fig. 5a). Upon initial discharge, the first peak at 2.33 V corresponds to the open ring reduction of cyclic S_8 to higher-order Li polysulfides (Li_2S_n, $8 > n > 4$), and the second peak at 2.07 V is associated with the formation of insoluble lower-order Li polysulfides (Li_2S_n, $n \leq 2$).[56,57] The subsequent anodic scan reveals two oxidation peaks at about 2.27 and 2.33 V. The peak at 2.27 V is associated with the oxidation of lower-order polysulfides to Li_2S_n ($n > 2$), which continues until the elemental sulfur is produced at 2.33 V.[56] Notably the PCN-S/RGOAs composite shows promised polarization reduction probably due to the incorporation of a highly conductive 3D graphene aerogel wrapping which can significantly enhance the redox activity of lithium polysulfides. Of course, the detailed mechanisms of the RGOAs nanosheets in the PCN-S/RGOAs hybrid still need to be further clarified in future work.

Compared with the PCN-S/RGOAs hybrid, PCN-S (Fig. S6†) and pristine sulfur (Fig. 5b) show similar patterns but have more prominent voltage polarization and much lower repeatability, presumably due to their poor conductivity and severe shuttle effect, which is further evidenced by the cycling performance (Fig. S7 and S8†). At 0.2 C (1 C = 1675 mA g^{-1}), the sulfur baseline (Fig. S7†) shows a discharge capacity of 1098 mA h g^{-1} in the first cycle and suffers severe, irreversible capacity loss and shuttle effect. Incorporating mesoporous PCN greatly improved cyclability (Fig. S8†). A discharge capacity as high as 1319 mA h g^{-1} is obtained in the first cycle but it gradually decreased to 609 mA h g^{-1} after 100 cycles, corresponding to a capacity loss of 54%. Notice that both the pristine sulfur and PCN-S electrodes show a capacity increase in the first few cycles before gradual degradation, probably due to their relatively poor conductivity, which takes a few cycles to fulfill the activation process. In contrast, the PCN-S/RGOAs hybrid shows a much more stable cycling performance over 300 cycles (Fig. 5c). In the first cycle, the PCN-S/RGOAs hybrid delivers a discharge capacity of 1328 mA h g^{-1} and a high Coulombic efficiency of 98%. After 300 cycles, a discharge capacity of 647 mA h g^{-1} is retained with a Coulombic efficiency close to 100% (Fig. 5c), indicating that the design architecture of highly conductive 3D graphene-aerogel-wrapped porous carbon nanosheets successfully alleviates the shuttling effect by trapping the polysulfides and inhibiting their dissolution into the electrolyte, thereby leading to a higher use of active sulfur and more stable cycling performance.

Moreover, the PCN-S/RGOAs hybrid demonstrates superior rate capability at discharge/charge rates ranging from 0.2 C to 8 C over 100 cycles (Fig. 5d and S9†). At the current rate of 0.2 C, the highest discharge capacity of 1352 mA h g^{-1} is achieved. The capacity decreases gradually with the increasing discharge/charge rate. The hybrid exhibits reversible capacities of 869 mA h g^{-1} for the 30th cycle at 1 C, 512 mA h g^{-1} over 30 cycles (42 to 71) at 8 C, corresponding to 66%, and 39% of the discharge capacity for the second cycle at 0.2 C, respec-

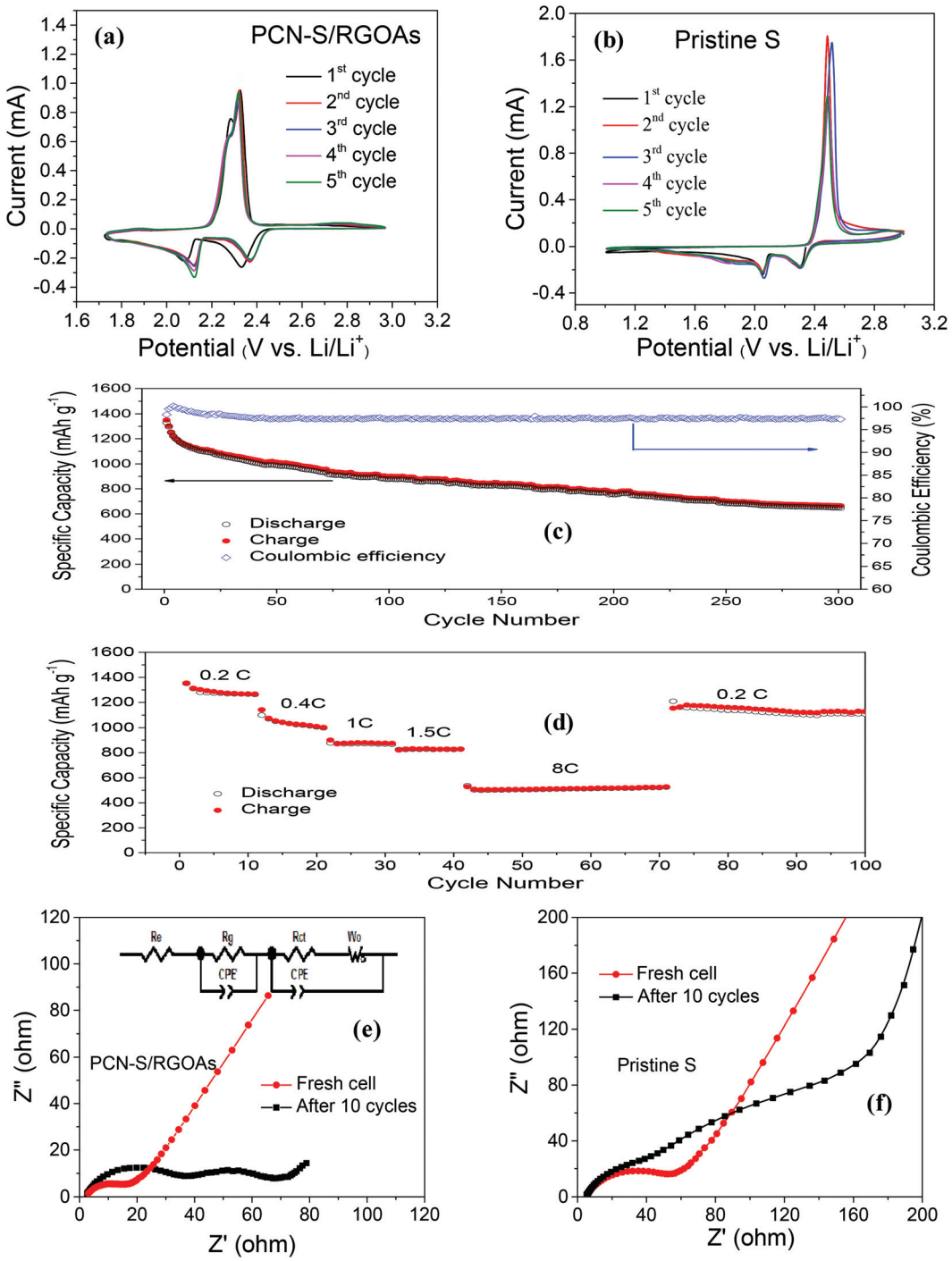

Fig. 5 (a) Cyclic voltammograms (CV) of the PCN-S/RGOAs between 1.7 V and 3.0 V at a scan rate of 0.1 mV s^{-1}, (b) CV curves of the pristine S between 1.0 V and 3.0 V at a scan rate of 0.1 mV s^{-1}, (c) charge–discharge cycling of the PCN-S/RGOAs at a current of 0.2 C between 1.7 and 3.0 V, and (d) rate performance with varying current from 0.2 C to 8 C in the same voltage range. Nyquist plots of (e) PCN-S/RGOAs (inset shows the equivalent circuit) and (f) pristine sulfur electrode before and after 10 cycles.

tively. When the current density changes back to 0.2 C at the 72nd cycle, it reveals a stable charge capacity of 1128 mA h g^{-1} for another 28 cycles. Compared with previous reports, our PCN-S/RGOAs hybrid shows superior electrochemical performance in terms of cyclability and rate capability (Table S1†). As a control, the PCN-S composite achieves only an average discharge capacity of 491 mA h g^{-1} at an 8 C rate over 20 cycles (Fig. S10†). The improved electrochemical performance of the PCN-S/RGOAs hybrid in terms of the cyclability and rate capability is presumably due to the combined merits of PCN and highly conductive 3D graphene networks: (a) the PCN with a high BET specific surface area and pore volume (1036 m^2 g^{-1}

and 0.806 cm^3 g^{-1}, Fig. S5†) provides a superior host for soluble polysulfides during discharge/charge processes, which dramatically reduces the shuttle effect and improves the active material utilization; (b) incorporating highly conductive 3D graphene networks can not only increase the conductivity but also accommodate the volume change and maintain the structural integrity.

Electrochemical impedance spectra (EIS) were used to gain further insights into the cycling stability and high-rate capability, which are mainly related to the interfacial charge-transfer process and ion diffusion in the active material.[58] Nyquist plots of the PCN-S/RGOAs hybrid (Fig. 5e, inset shows equivalent circuits) and pristine sulfur (Fig. 5f and S11†) as the cathode electrode before cycling consist of one semicircle, which is associated with the charge transfer resistance (R_{ct}) of the cell. After 10 cycles, appearance of the semicircle at the high frequency region can be ascribed to the accumulated passivation layer on the electrode surface.[59,60] The semicircle in the medium-frequency region is associated with charge transfer resistance at the electrode–electrolyte interface. The inclined tail in the low-frequency region is ascribed to the ion diffusion within the electrodes.[61,62] Notice that the PCN-S/RGOAs hybrid consistently shows less resistance in charge-transfer and ion diffusion, which further confirms our assumption that the unique structural design of PCN-S/RGOAs can significantly improve the electrical conductivity and ultimately lead to superior electrochemical performance.

4. Conclusions

In summary, a novel dual-confined cathode is designed for Li–S batteries by embedding the sulfur encapsulated within 2D PCN into graphene aerogel networks. In addition to largely increasing the amount of sulfur loading, the porous structure of the 2D PCN can accommodate the volume expansion of sulfur during cycling and physically confine polysulfide intermediates. The graphene aerogel provides efficient 3D conductive networks for electron transfer, open channels for ion diffusion, and accessibility for electrolyte infiltration. Furthermore, graphene sheets embedded in the PCN-S act as a second protective layer to stabilize the sulfur of the active material; as a result, the obtained PCN-S/RGOAs hybrid exhibits excellent electrochemical performance with a high reversible capacity of 1328 mA h g^{-1}, superior coulombic efficiency (up to 100%) and rate capability, and outstanding cycling stability (the reversible capacity remains as large as 647 mA h g^{-1} at 0.2 C after 300 cycles). With further rational optimization, the reported dual-confined electrodes may hold great promise for the development of high-performance Li–S batteries.

Acknowledgements

Financial support for this work was provided by the U.S. Department of Energy (DE-EE0003208) and the Research Growth Initiative Program of the University of Wisconsin-Milwaukee (UWM).

Notes and references

1 P. G. Bruce, S. A. Freunberger, L. J. Hardwick and J. Tarascon, *Nat. Mater.*, 2012, **11**, 172–172.
2 X. Yang, L. Zhang, F. Zhang, Y. Huang and Y. Chen, *ACS Nano*, 2014, **8**, 5208–5215.
3 M. Q. Zhao, Q. Zhang, J. Q. Huang, G. L. Tian, J. Q. Nie, H. J. Peng and F. Wei, *Nat. Commun.*, 2014, **5**, 3410.
4 Z. W. Seh, J. H. Yu, W. Li, P. C. Hsu, H. Wang, Y. Sun, H. Yao, Q. Zhang and Y. Cui, *Nat. Commun.*, 2014, **5**, 5017.
5 M. Gong, Y. Li, H. Wang, Y. Liang, J. Z. Wu, J. Zhou, J. Wang, T. Regier, F. Wei and H. Dai, *J. Am. Chem. Soc.*, 2013, **135**, 8452–8455.
6 V. Etacheri, R. Marom, R. Elazari, G. Salitra and D. Aurbach, *Energy Environ. Sci.*, 2011, **4**, 3243–3262.
7 J. Liu, W. Li, L. Duan, X. Li, L. Ji, Z. Geng, K. Huang, L. Lu, L. Zhou, Z. Liu, W. Chen, L. Liu, S. Feng and Y. Zhang, *Nano Lett.*, 2015, **15**, 5137–5142.
8 X. Liang, A. Garsuch and L. F. Nazar, *Angew. Chem., Int. Ed.*, 2015, **54**, 3907–3911.
9 Q. Pang, D. Kundu, M. Cuisinier and L. F. Nazar, *Nat. Commun.*, 2014, **5**, 4759.
10 Y. X. Yin, S. Xin, Y. G. Guo and L. J. Wan, *Angew. Chem., Int. Ed.*, 2013, **52**, 13186–13200.
11 X. Liang, C. Hart, Q. Pang, A. Garsuch, T. Weiss and L. F. Nazar, *Nat. Commun.*, 2015, **6**, 5682.
12 L. Zhuang, Y. Yuan, G. Yang and S. Zhou, *Electrochem. Commun.*, 2012, **21**, 69–72.
13 H. Chen, C. Wang, Y. Dai, S. Qiu, J. Yang, W. Lu and L. Chen, *Nano Lett.*, 2015, **15**, 5443–5448.
14 J. Zhang, Z. Dong, X. Wang, X. Zhao, J. Tu, Q. Su and G. Du, *J. Power Sources*, 2014, **270**, 1–8.
15 S. Evers and L. F. Nazar, *Acc. Chem. Res.*, 2013, **46**, 1135–1143.
16 Z. Zhang, Z. Li, F. Hao, X. Wang, Q. Li, Y. Qi, R. Fan and L. Yin, *Adv. Funct. Mater.*, 2014, **24**, 2500–2509.
17 W. Li, G. Zheng, Y. Yang, Z. W. Seh, N. Liu and Y. Cui, *Proc. Natl. Acad. Sci. U. S. A.*, 2013, **110**, 7148–7153.
18 X. Pu, G. Yang and C. Yu, *Adv. Mater.*, 2014, **26**, 7456–7461.
19 Z. Li, Y. Jiang, L. Yuan, Z. Yi, C. Wu, Y. Liu, P. Strasser and Y. Huang, *ACS Nano*, 2014, **8**, 9295–9303.
20 G. Zhou, Y. Zhao and A. Manthiram, *Adv. Energy Mater.*, 2015, **5**, 1402263.
21 G. He, S. Evers, X. Liang, M. Cuisinier, A. Garsuch and L. F. Nazar, *ACS Nano*, 2013, **7**, 10920–10930.
22 W. Xia, B. Qiu, D. Xia and R. Zou, *Sci. Rep.*, 2013, **3**, 1935.
23 K. Xi, S. Cao, X. Peng, C. Ducati, R. Vasant Kumar and A. K. Cheetham, *Chem. Commun.*, 2013, **49**, 2192–2194.
24 J. Zhang, J. Xiang, Z. Dong, Y. Liu, Y. Wu, C. Xu and G. Du, *Electrochim. Acta*, 2014, **116**, 146–151.
25 N. Jayaprakash, J. Shen, S. S. Moganty, A. Corona and L. A. Archer, *Angew. Chem., Int. Ed.*, 2011, **50**, 5904–5908.

26 C. Zhang, H. B. Wu, C. Yuan, Z. Guo and X. W. Lou, *Angew. Chem., Int. Ed.*, 2012, **51**, 9592–9595.
27 J. Schuster, G. He, B. Mandlmeier, T. Yim, K. T. Lee, T. Bein and L. F. Nazar, *Angew. Chem., Int. Ed.*, 2012, **51**, 3591–3595.
28 X. A. Chen, Z. Xiao, X. Ning, Z. Liu, Z. Yang, C. Zou, S. Wang, X. Chen, Y. Chen and S. Huang, *Adv. Energy Mater.*, 2014, **4**, 1301988.
29 J. Hou, C. Cao, F. Idrees and X. Ma, *ACS Nano*, 2015, **9**, 2556–2564.
30 B. Wang, W. Al Abdulla, D. Wang and X. S. Zhao, *Energy Environ. Sci.*, 2015, **8**, 869–875.
31 X. Y. Zhao, J. P. Tu, Y. Lu, J. B. Cai, Y. J. Zhang, X. L. Wang and C. D. Gu, *Electrochim. Acta*, 2013, **113**, 256–262.
32 Y. Zhao, C. Hu, L. Song, L. Wang, G. Shi, L. Dai and L. Qu, *Energy Environ. Sci.*, 2014, **7**, 1913–1918.
33 S. Nardecchia, D. Carriazo, M. L. Ferrer, M. C. Gutierrez and F. del Monte, *Chem. Soc. Rev.*, 2013, **42**, 794–830.
34 B. Qiu, M. Xing and J. Zhang, *J. Am. Chem. Soc.*, 2014, **136**, 5852–5855.
35 L. Wang, D. Wang, F. Zhang and J. Jin, *Nano Lett.*, 2013, **13**, 4206–4211.
36 S. Jing, H. Jiang, Y. Hu, J. Shen and C. Li, *Adv. Funct. Mater.*, 2015, **25**, 5395–5401.
37 C. Xu, Y. Wu, X. Zhao, X. Wang, G. Du, J. Zhang and J. Tu, *J. Power Sources*, 2015, **275**, 22–25.
38 Z. Li, J. Ding, H. Wang, K. Cui, T. Stephenson, D. Karpuzov and D. Mitlin, *Nano Energy*, 2015, **15**, 369–378.
39 S. Han, J. Jiang, Y. Huang, Y. Tang, J. Cao, D. Wu and X. Feng, *Phys. Chem. Chem. Phys.*, 2015, **17**, 1580–1584.
40 Y. Hou, J. Li, Z. Wen, S. Cui, C. Yuan and J. Chen, *Nano Energy*, 2014, **8**, 157–164.
41 Y. Hou, Z. Wen, S. Cui, X. Guo and J. Chen, *Adv. Mater.*, 2013, **25**, 6291–6297.
42 J. Zhou, J. Qin, X. Zhang, C. Shi, E. Liu, J. Li, N. Zhao and C. He, *ACS Nano*, 2015, **9**, 3837–3848.
43 M. Sevilla and A. B. Fuertes, *ACS Nano*, 2014, **8**, 5069–5078.
44 W. S. Hummers and R. E. Offeman, *J. Am. Chem. Soc.*, 1958, **80**, 1339–1339.
45 G. Zhou, E. Paek, G. S. Hwang and A. Manthiram, *Nat. Commun.*, 2015, **6**, 7760.
46 H. Wang, Z. Xu, H. Yi, H. Wei, Z. Guo and X. Wang, *Nano Energy*, 2014, **7**, 86–96.
47 Y. Hou, T. Huang, Z. Wen, S. Mao, S. Cui and J. Chen, *Adv. Energy Mater.*, 2014, **4**, 1400337.
48 H. Hu, H. Cheng, Z. Liu, G. Li, Q. Zhu and Y. Yu, *Nano Lett.*, 2015, **15**, 5116–5123.
49 Y. Hou, F. Zuo, Q. Ma, C. Wang, L. Bartels and P. Feng, *J. Phys. Chem. C*, 2012, **116**, 20132–20139.
50 R. Chen, T. Zhao, J. Lu, F. Wu, L. Li, J. Chen, G. Tan, Y. Ye and K. Amine, *Nano Lett.*, 2013, **13**, 4642–4649.
51 A. Manthiram, Y. Fu, S. H. Chung, C. Zu and Y. S. Su, *Chem. Rev.*, 2014, **114**, 11751–11787.
52 Z. Wang, Y. Dong, H. Li, Z. Zhao, H. Bin Wu, C. Hao, S. Liu, J. Qiu and X. W. Lou, *Nat. Commun.*, 2014, **5**, 5002.
53 Y. Hou, Z. Wen, S. Cui, S. Ci, S. Mao and J. Chen, *Adv. Funct. Mater.*, 2015, **25**, 872–882.
54 G. Zhou, L. C. Yin, D. W. Wang, L. Li, S. Pei, I. R. Gentle, F. Li and H. M. Cheng, *ACS Nano*, 2013, **7**, 5367–5375.
55 Y. Hou, B. Zhang, Z. Wen, S. Cui, X. Guo, Z. He and J. Chen, *J. Mater. Chem. A*, 2014, **2**, 13795–13800.
56 N. Jayaprakash, J. Shen, S. S. Moganty, A. Corona and L. A. Archer, *Angew. Chem., Int. Ed.*, 2011, **50**, 5904–5908.
57 J. Tian, Q. Liu, N. Cheng, A. M. Asiri and X. Sun, *Angew. Chem., Int. Ed.*, 2014, **53**, 9577–9581.
58 G. C. Li, G. R. Li, S. H. Ye and X. P. Gao, *Adv. Energy Mater.*, 2012, **2**, 1238–1245.
59 J. Zheng, M. Gu, H. Chen, P. Meduri, M. H. Engelhard, J. G. Zhang, J. Liu and J. Xiao, *J. Mater. Chem. A*, 2013, **1**, 8464–8470.
60 J. Kim, D. J. Lee, H. G. Jung, Y. K. Sun, J. Hassoun and B. Scrosati, *Adv. Funct. Mater.*, 2013, **23**, 1076–1080.
61 D. W. Wang, G. Zhou, F. Li, K. H. Wu, G. Q. Lu, H. M. Cheng and I. R. Gentle, *Phys. Chem. Chem. Phys.*, 2012, **14**, 8703–8710.
62 J. Wang, S. Y. Chew, Z. W. Zhao, S. Ashraf, D. Wexler, J. Chen, S. H. Ng, S. L. Chou and H. K. Liu, *Carbon*, 2008, **46**, 229–235.